# Revealing meso-structure dynamics in additive manufacturing of energy storage via *operando* coherent X-ray scattering

Cheng-Hung Lin [a,#], Karol Dyro [b,#], Olivia Chen [a], Dean Yen [a], Bingqian Zheng [c], Maria Torres Arango [e], Surita Bhatia [c], Ke Sun [a], Qingkun Meng [d,a], Lutz Wiegart [e,**], Yu-chen Karen Chen-Wiegart [a,e,*]

[a] Department of Materials Science and Chemical Engineering, Stony Brook University, Stony Brook, NY 11794, USA
[b] Department of Physics, Stony Brook University, Stony Brook, NY 11794, USA
[c] Department of Chemistry, Stony Brook University, Stony Brook, NY 11794, USA
[d] School of Materials Science and Physics, China University of Mining and Technology, Xuzhou 221116, China
[e] National Synchrotron Light Source II, Brookhaven National Laboratory, Upton, NY 11973, USA

## ARTICLE INFO

## ABSTRACT

3D printing is an emerging technology for the fabrication of energy storage devices, offering advantages over traditional manufacturing methods. However, optimization and design of such devices requires an understanding of the meso–structure formation during the 3D printing process. This study utilizes *operando* coherent X-ray scattering, X-ray Photon Correlation Spectroscopy (XPCS), to study the spatiotemporally-resolved far-from-equilibrium dynamics during direct ink writing 3D printing. Lithium Titanate (LTO) based ink is prepared and rheologically tested for its shear-thinning properties. Two-time intensity-intensity functions are calculated to be used in subsequent quantitative analysis, which allows for an overall characterization of the dynamics, description of an initial fast decorrelation and identification of sudden rearrangements of subdomains of the sample. The results show the dynamics to be anisotropic, spatiotemporally heterogenous and marked by distinct rearrangement events, all of which impact the electrochemical performance of energy storage devices. The studied 3D printing ink is used to fabricate electrodes which are then electrochemically tested, showing good performance in cycling and retaining structural integrity. This work furthers the understanding of the far-from-equilibrium material dynamics during 3D printing, giving quantitative characterization of this process, and highlights aspects of structure formation relevant to the electrochemical performance of the resultant energy storage device.

© 2021 Published by Elsevier Ltd.

## 1. Introduction

3D printing, also known as additive manufacturing, has revolutionized how materials are being manufactured into complex architectures. This rapidly evolving technology offers great opportunities to design energy storage systems with controlled and adaptable spatial geometry and with enhanced performance and functionalities. Specifically, 3D printing is particularly promising for future energy harvesting [1,2] and storage micro-devices [3–6] with significant benefits [4,7,8] including: 1) Versatility: A storage device of arbitrary shape can be printed for flexible electronics, wearable electronics and smart fabrics [9]. 2) Performance: Unique architectures can effectively reconcile high-rate performance and high energy density, leading to enhanced performance [10,11]. 3) Integration: Power sources can be directly embedded into the 3D printed structure and devices, such as sensors and electronics [12,13]. However, 3D printing strategies only offer complex architectural designs on the macroscopic scale. The batteries' performance is critically determined by the mesoscale structure within the printed filaments, which remains difficult to control, due to a significant lack of understanding of the processes involved in structure formation. There is a great research need to understand the non-equilibrium processing - mesoscale structure relationship for 3D printed batteries and to control the mesoscale structures through highly non-equilibrium processing conditions.

Amongst different 3D printing technologies, the extrusion-based continuous-flow direct ink writing method attracts great attention with a broad range of applications across multiple fields

---

[14]. As the colloidal ink can be prepared via physical mixing and thus does not depend on specific chemical synthesis conditions [15,16], direct ink writing remains as one of the most versatile methods [9], allowing printing various materials required for 3D printed batteries and multi-materials integration [17]. In most direct ink writing processes, colloidal viscoelastic inks are being extruded via a nozzle, undergoing shear-thinning. The liquid-like materials can then be deposited directly onto a substrate, and dynamically recover to support the layer-by-layer construction of complex architectures. Inks used in 3D printing batteries or other micro-devices by direct ink writing typically consist of active functional particles, conductive carbon, rheology-tuning agents such as polymers, and curing-agents such as solvents [15,18–23]. Since the initial demonstration of 3D printed lithium ion batteries [4], various cathode and anode materials and different energy storage systems have been developed with direct ink writing. These include printing various carbon-based materials for supercapacitors [24,25], lithium metal oxides for Li-ion batteries [3,4,26–30], and beyond Li-ion batteries [31–33].

The current 3D printing battery developments focus on demonstrating better charge/discharge capacities and cycle performance than conventional batteries with flat electrodes. Carbon additives, such as graphene oxide, were added to make composite inks to explore the possibility of increasing the electrical conductivity while maintaining the physical properties such as shear thinning behavior [34]. Charging and discharging 3D printed Li-ion batteries kinetics have been studied and applied to Li-ion diffusion paths, therefore increasing the redox potentials of a 3D printed cathode [35]. The structural integrity of 3D printed battery electrode during and after printing through a nozzle were further developed especially in 3D-structured electrodes instead of the traditional laminated structures [27]. More recently, adding Ketjenblack carbon particles has been integrated into 3D printed electrodes in electrolyte solutions that are lithium based [36]. Cathode materials for Li-ion batteries have been printed with macropores, increasing the opportunities for electrolyte penetration with polymer networks that allow for ion and electron movement [37]. These examples showed that in the last several years studies on additive manufacturing have been rapidly exploring numerous facets of 3D printed batteries' physical and electrochemical properties.

However, 3D printing is inherently complex, both in terms of the materials and processes involved. Due to this complexity, our understanding of materials' behavior under 3D printing processing conditions remains limited. Specifically, the deposition process in direct ink writing is driving the materials into a highly non-equilibrium state via shearing and solvent-evaporation. Therefore, controlling the internal structure during the highly non-equilibrium processes in 3D printing remains challenging and highly empirical due to the lack of understanding of the dynamic processes in mesoscale morphological evolution. This impacts the requirements in battery design, where tailoring materials micro-/meso–structure to better control the ionic and electron transfer through a dynamic chemical environment is the key to desired performance [38]. Strategies to change materials micro-/meso–structure [3,13,31,32,39,40] highlight the importance of a better understanding in order to control the internal mesoscale structure when attempting to utilize the new 3D printing method to create 3D printed batteries.

In this work, we utilized X-ray photon correlation spectroscopy (XPCS) to address the dynamics of mesoscale structure formation during the far-from-equilibrium processes of 3D printing of energy storage electrode materials. Hard X-ray scattering is a technique well suited for investigating 3D printing processes and incoherent scattering has been applied to study in-situ polymer crystallization [41,42] as well as filler morphology in 3D printed epoxy-nanoclay-carbon fiber composites [43]. In XPCS, a time-dependent,

disordered system is probed with partially coherent X-rays, and the interference between the coherently scattered waves produces a time-evolving series of speckle patterns. In addition to time-resolved structural information, like small angle X-ray scattering (SAXS), that is accessible by incoherent scattering techniques, XPCS resolves fluctuations of the nanoscale structure around its average configuration via time-series of coherent speckle patterns. The technique thus allows probing phenomena that are not accessible with incoherent scattering techniques. A wide variety of dynamic phenomena can be quantitatively measured by analyzing the temporal correlation of the speckle intensities in XPCS, [44] including colloids [45–49], aging phenomena in soft-matters [50–52], rheology of materials under flow [52–55], self-organization [65], structural and dynamical properties of polymers and polymer-nanocomposites [56,57,58,59,60,61,62], including industrially relevant systems [63] and under mechanically induced strain [64]. These phenomena can be critical in the meso–structural evolution in 3D printing during both the deposition and structural recovery processes. A recent development at the Coherent Hard X-ray (CHX) beamline of the National Synchrotron Light Source II (NSLS-II) enabled the *operando* study of 3D printing processes using XPCS, providing temporospatially resolved information about the nanoscale structural and dynamic evolution [66]. However, to-date, the systems studied have been limited to model mono-disperse systems [67], commercial thermoset [68], UV-cured epoxy-based nanocomposites [67] and ceramics [69]. This work attempts to first apply XPCS to further the understanding of the out-of-equilibrium processing pathways in 3D printing batteries, with an ultimate goal towards guiding a rational design for the next generation energy storage materials. The work also applies a viscosifier (rheology tuning polymer), sodium carboxymethyl cellulose (SCC), compatible with the electrolyte of Li-ion batteries, such that the polymer does not need to be converted to carbon via heating under high temperature (600 °C), significantly simplifying the ink processing. Instead, carbon additives can be readily added as part of the ink formulation. The dynamics of printing the complex multi-phase fluid probed by XPCS hopefully will lead to greater impacts on a broad range of technologies.

## 2. Methods

### 2.1. Ink preparation

As shown in Fig. S 1 (b), the 3D printable inks were prepared by first creating a mixture of 4.5 g Lithium Titanate (LTO) powder (Sigma Aldrich, USA), 40 mL of Ethylene Glycol (Sigma Aldrich, USA), and 110 mL of deionized water [70]. The starting solution underwent 24 h of ball milling to well disperse LTO particles in the solution. The solution was then centrifuged (Eppendorf 5804) with a relative centrifugal force (RCF) of 1575 g for 99 min. Effluent was then removed from the centrifuged solution, leaving behind 2–4 ml of solution containing particles. The particle-containing solution was then mixed using an electrical mixer (Vortex mixer, Fisherbrand, USA) vortexed in the remaining effluent. The LTO wt.% in the well mixed solution was determined by the following steps. 6–10 drops of solution were pipetted onto a microscope slide, which was then heated on a plate to 200 °C to evaporate the liquids in the solution. The slide was cooled down once there was no more evaporation of solvents. The mass of the solution before and after drying was measured to calculate the wt.% of LTO in the solution; this value is required to determine the quantity of additives and active material in the 3D printable ink.

Sodium Carboxymethyl Cellulose (SCC, from Sigma Aldrich, USA) was used as viscosifier during the ink synthesis. The SCC powder was diluted in deionized water to make a 3 wt.% solution for pre-dispersion. The conductive additive was carbon black solu-
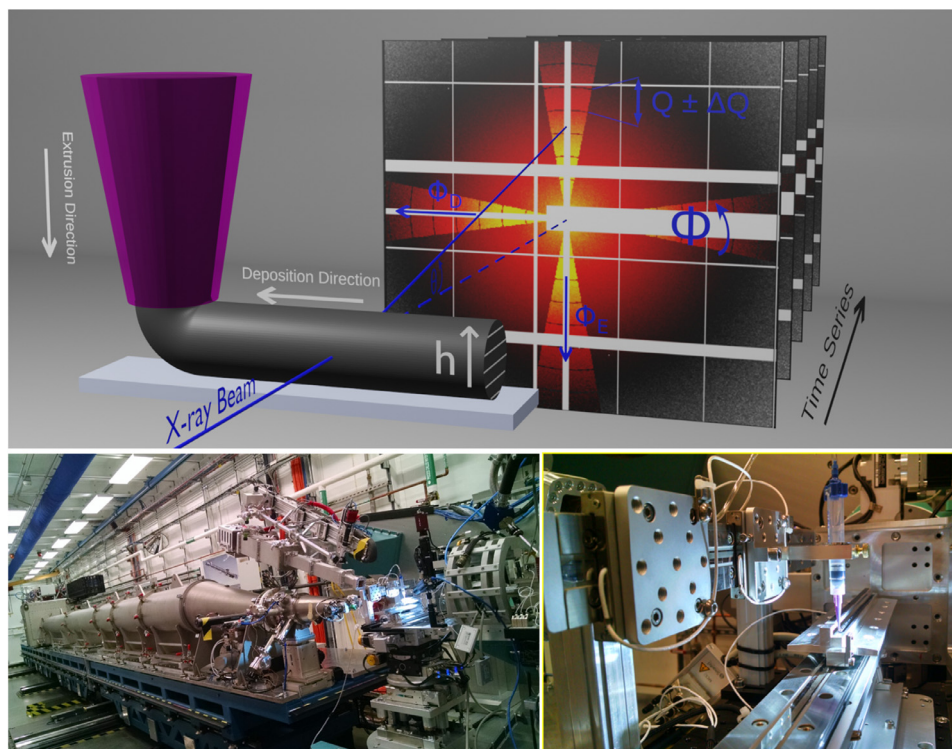
**Fig. 1.** Time-resolved coherent X-ray scattering experimental setup: (a) Schematic of the setup portraying a nozzle extruding LTO printable battery electrode ink onto a Si substrate. An example path of a scattered X-ray beam is shown in solid blue with the dashed blue line representing the transmitted beam. The beam is incident on a plane depicting the averaged scattering pattern. The triangular shapes show the region over which angular resolved correlation functions were calculated to resolve the dynamics for extrusion and deposition directions. (b) Experimental setup photographed at the CHX beamline, NSLS-II showing an overview of the end-station, with close view of the printing setup. The print head with 3D printable LTO ink in the syringe is marked with a green rectangle.

tion prepared by mixing 1 g of carbon black (Timical Super C65, MTI Corporation), 0.754 g of SCC powder, 40 mL of ethylene glycol, and 110 mL of deionized water. The carbon black mixture was ball milled for 24 h and centrifuged with RCF 3214 g for 10 min to remove large agglomerates, followed with RCF 1575 g for 99 min to collect fine particles. The remaining solution containing carbon black particles was then mixed with an electrical mixer, and the wt.% of the carbon black in the solution was also determined following the same procedure as for LTO. An ink precursor was prepared by homogenizing the LTO mixture, 10 wt.% SCC, 11.8 wt% carbon black, 27% glycerol, and solvent (ethylene glycol and water) by a planetary mixer (THINKY centrifugal mixer ARM-310, Thinky USA). The wt.% of additives were relative to the LTO solid content. A drying process was applied to the ink precursor to obtain a final solid loading, wt.% of total solid contents in 3D printing ink, ~36% through solvent evaporation at 60 °C in air. The solvent evaporation was conducted at room temperature and the ink was homogenized by the planetary mixer periodically. The final ink composition (in wt.%) includes LTO: 29.6%, SCC: 3.3%, carbon:3.2%, water: 33.0%, ethylene glycol: 30.0%.

### 2.2. Ink morphology and rheology characterization

The particle morphology of the LTO powder was imaged by Scanning Electron Microscopy (JEOL 7600F) at the Center for Functional Nanomaterials (CFN) at Brookhaven National Laboratory (BNL). Dynamic Light Scattering (DLS) (Brookhaven Instruments NanoBrook Omni Dynamic Light Scattering) was used to quantify the particle size distribution in the ink. The DLS samples for the LTO particles were taken from the LTO mixture after being centrifuged and diluted 500 times in deionized water. The rheological

behavior of synthetic inks was analyzed using a Discovery HR-3 rheometer (TA Instruments) at CFN, BNL, with a 20-mm diameter 1.969° cone steel Peltier plate at 25 °C. The shear storage ($G'$) and loss ($G''$) moduli were collected as a function of shear stress (10 – 3000 Pa) in an oscillation amplitude mode with a frequency of 1 Hz in logarithmic sweep. The viscosity data were measured as a function of shear rate (0.01 to 500 $s^{-1}$) in a logarithmically flow sweep mode.

### 2.3. In situ printing experiment with time-resolved coherent X-ray scattering

The printing experiment with *in situ* time-resolved coherent X-ray scattering was conducted at the CHX beamline (11-ID) of NSLS-II, Brookhaven National Laboratory. An in-house built extrusion-based direct ink writing printer was used *operando* to study the behavior of 3D printable electrode inks [66]. A schematic illustrating the experimental setup is shown in Fig. 1. The experiment characterized the printing processes including the deposition and the consecutive material recovery.

3D printable electrode inks were deposited using a pressure-controlled syringe-piston system (Ultimus V, Nordson) as part of the printer setup, with a 580 μm inner diameter conical nozzle. The extrusion pressure was set to 50 psi and the printing velocity was set to 0.5 mm s$^{-1}$. A silicon substrate was used as the deposition substrate and an initial test print was used to optimize the setup, including determining permissible radiation dose, data acquisition parameters and height of the filament; the surface of the substrate and the height of the printed filament were determined via absorption scans. To ensure the results are dose independent, the effects of dose on the measured dynamics and struc-

ture were analyzed systematically, according to an established procedure [71]. For the samples used in this study, a dose limit corresponding to ≈5 s of exposure with the unattenuated beam at a flux of $2 \times 10^{11}$ photons per second was established. The radiation dose received by the samples during data acquisition was controlled by a millisecond shutter and an attenuator system based on double-sided polished silicon wafers.

To conduct the time-resolved coherent X-ray scattering experiment, a partially coherent X-ray beam was used, with the incident X-ray energy set to 9.647 keV. The X-ray beam was focused by refractive optics to a $10 \times 10$ μm² beam cross-section (full width at half maximum, FWHM) at the sample position. Coherent X-ray scattering patterns were collected using a photon-counting pixelated area detector (Eiger X 4 M, Dectris Inc.) with frame rates up to 750 Hz. During the *in situ* printing experiment, the printhead of the printer was moved along the deposition direction (Fig. 1), keeping the print-bed and deposited filament stationary during data acquisition. The X-ray data acquisition started prior to the printhead crossing the X-ray beam and thus captured the scattering intensity rise associated with the filament being deposited across the beam, which is defined as the on-set of printing time, defined as $t_{age} = 0$ s [71].

The filaments were probed *in situ* by the X-ray beam at 5 different heights (h) evenly distributed from the near-substrate position (30 μm from the substrate surface) to top of the filament. At each height, four scans were collected at different sample ages to characterize different stages of the printing processes. The first two scans were measured during *in situ* printing, collected with two different exposure times to capture the dynamics at different timescales. These scans are labeled as "in-situ-fast" (1.34 ms per frame), and "in-situ-slow" (50 ms per frame). Each scan's total dose was kept lower than the previously characterized dose threshold level; consequentially, the in-situ-fast scans captured ~ 5.4 s of the printing process, whereas the in-situ-slow scans captured ~150 s. Following the in-situ slow scan, two additional post-printing scans were conducted on the as-printed electrode filament to capture the dynamics during the recovery phase shortly after printing. Labeled as "post-printing-1" (followed right after the in-situ-slow scan) and "post-printing-2" (5 min after printing) scans, both post-printing scans were collected under the same rate as the in-situ-slow scan. The sample position was shifted by 50 μm horizontally between these consecutive scans (in-situ slow, post-printing-1, post-printing 2) to avoid accumulation of X-ray dose. The deposition process was also monitored via several optical cameras during the *in situ* X-ray experiment.

### 2.4. Electrochemical testing

For comparison, LTO electrodes were prepared by both 3D printing and conventional blade casting. For the electrodes prepared by printing, single and triple-layered patterns of LTO electrodes were printed using the same in-house built printer used during the *in situ* coherent X-ray scattering experiment with a 200-μm conical nozzle to optimize the electrochemical performance. The conventionally casted electrodes were prepared by casting the LTO ink on aluminum foil (MTI Corporation) through an adjustable film coating doctor blade (MTI Corporation) with a gap of 200 μm. Electrochemical performance of synthetic LTO ink was carried out with CR2032 coin cells assembled in an argon-filled glove box. For each coin cell, a Celgard membrane was used as the separator and a disk of lithium metal was used as the counter and reference electrode. The electrolyte (MTI Corporation) was 1 M LiPF6 dissolved in EC:EMC with a volume ratio of 3:7. Electrochemical charge/discharge tests were performed with a potentiostat (VSP300, Bio-Logic) in a voltage window from 1 V to 2 V (vs Li$^+$/Li) by galvanostatic cycling.

## 3. Results and discussions

### 3.1. Ink and printed structure characterization

The formulated LTO electrode ink exhibits shear thinning behavior, as demonstrated by the rheology results shown in Fig. 2 (a-b). The viscosity of the ink reduces as a function of shear rate Fig. 2(a). The shear storage modulus (G′) and shear loss modulus (G″) show a transition from solid-like to liquid-like behavior as the shear stress increases, indicated by the crossover of G′ and G″ in Fig. 2(b). This shear thinning behavior enables the printing process as the solid-like ink turns liquid-like under shear during the ink deposition, and then recovers its solid-like behavior after deposition. A photograph of the 3D printable ink can be found in Fig. S 1(a) in the supporting information.

The surface morphology of the printed and cured LTO electrode was characterized by SEM imaging, shown in Fig. 2(c). The LTO particle size is uniformly distributed, with size ~ 100 nm. Small amount of LTO particle aggregates can be observed, consistent with the dynamic light scattering (DLS) results of the LTO particles obtained from centrifugation (Fig. S 1(b)). Larger carbon black additive particles are randomly distributed within the LTO network, enhancing the electrical conductivity.

### 3.2. In situ printing study by time-resolved X-ray scattering

The time series of coherent scattering patterns contain information about the evolution of the nanoscale structure of the filaments, identical to a time-resolved SAXS experiment. The SAXS curves are mostly featureless, except for a weak and broad structure factor peak arising from the average nearest neighbor distance of the LTO particles. The LTO particles itself are too polydisperse to give rise to any form factor oscillations. An example for the obtained SAXS curves and their analysis is shown in Fig. S 3. The structure factor was determined as $S(Q,t_{age},h)=I(Q,t_{age},h)/I_{dilute}(Q)$, where $I_{dilute}(Q)$ is the SAXS curve obtained by a dilute (2 wt.%) suspension of LTO particles. The nearest neighbor distance ($2\pi/Q_c$) and domain size ($2\pi/Q_c^{FWHM}$) are obtained by fitting $S(Q,t_{age})$ to a pseudo-Voigt profile with center $Q_c$ and corresponding FWHM $Q_c^{FWHM}$, shown in Fig. S 2 (a) and Fig. S 2 (b), respectively. The Porod regime of $I(Q,t_{age},h)$ were fitted with the power law $I(Q,t_{age},h) \propto Q^N$. The obtained exponent is plotted in Fig. S 2 (c). Here the nearest neighbor distance obtained in SAXS, 60–65 nm, corresponds to the particle-to-particle distance; this distance is less than the size distribution (peak ~ 100 nm), obtained in the DLS, which measures the size of the clusters formed by these primary particles.

The nanoscale dynamics of the ink during and shortly after printing a single filament was investigated using XPCS. The XPCS data analysis was carried out using Python-based software available at CHX beamline [72]. Based on the collected time-series of speckle patterns, two-time intensity-intensity correlation functions $G$ were calculated (separately for each filament height $h$) according to [73–75]:

$$G(Q, \Phi, t_1, t_2) = \frac{\langle I(t_1) \cdot I(t_2) \rangle_{Q,\Phi}}{\langle I(t_1) \rangle_{Q,\Phi} \cdot \langle I(t_2) \rangle_{Q,\Phi}}, \qquad (1)$$

where $<...>_{Q,\Phi}$ indicates an average over a range of detector pixels corresponding to wave vectors with amplitude centered around $Q$ ($\pm0.002$ Å$^{-1}$) and angles $\Phi$ ($\pm10°$) around the extrusion ($\Phi_E$) and deposition ($\Phi_D$) directions. The wavevector $Q$ in the employed SAXS geometry is defined as: $Q = 4\pi \sin(\theta/2)/\lambda$, where $\theta$ is the angle between the X-ray beam and the trajectory of the scattered radiation (Fig. 1) and $\lambda = 1.285$ Å is the wavelength of the incident X-rays. $I(t_{1/2})$ is the number of photons in a detector pixel at times $t_1$ and $t_2$, respectively. $t_1 = t_2 = 0$ s was determined in the
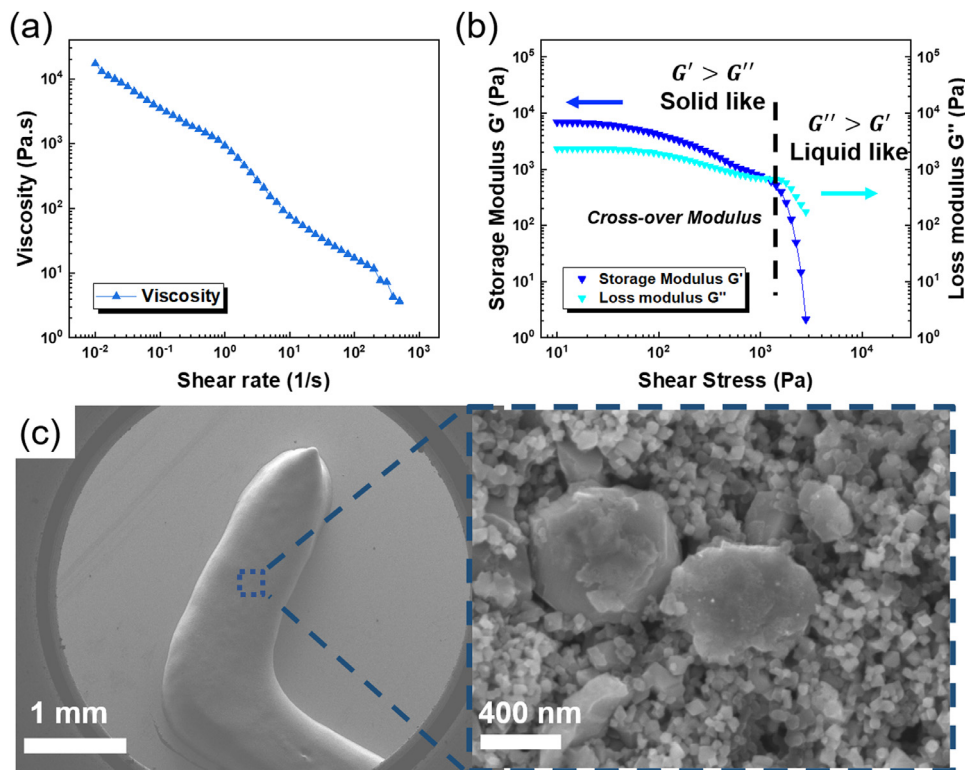
**Fig. 2.** LTO ink characterization: Rheology analysis of the ink showed a shear thinning behavior, including (a) viscosity vs. shear rate, and (b) the storage modulus and loss modulus vs. shear stress. (c) The SEM images of a single-layer printed LTO electrode structure after printing and curing, showing an overview of the surface and a zoom-in view of the particles within the printed electrode.
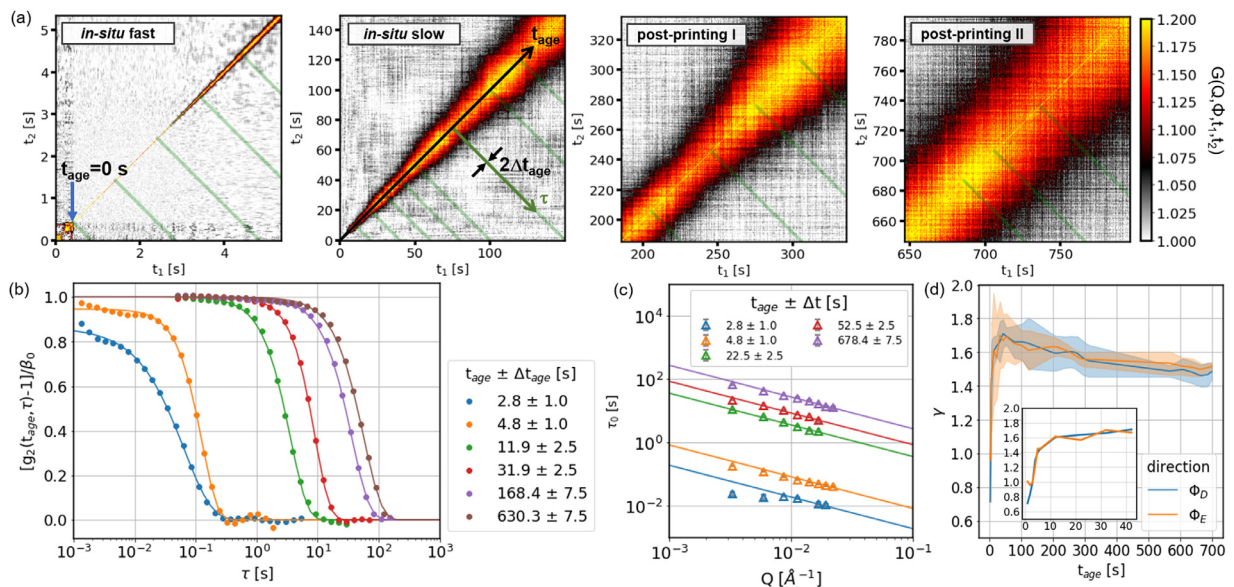


**Fig. 3.** (a) Examples of two-time correlation functions for the deposition direction ($\Phi=\Phi_D$) at a filament height $h = 270$ μm from two in-situ scans and two scans after deposition, respectively. Green lines represent the time slices used to produce the one-time correlation functions. (b) Normalized one-time correlation functions for different sample ages produced from the slices of two-time correlation functions for $Q = 0.00326$ Å$^{-1}$, $\Phi=\Phi_D$ and $h = 504$ μm. (c) Linear fits of the Q-dependence of the relaxation time for different ages for $\Phi=\Phi_D$ and $h = 504$ μm. (d) Height- and Q-averaged time evolution of the stretching exponent $\gamma$ for both the deposition ($\Phi_D$) and extrusion ($\Phi_E$) direction (shaded regions represent the standard deviation).

'in-situ' dataset by the intensity rise cause by the filament being deposited across the X-ray beam, corresponding to an average age time $t_{age}=(t_1+t_2)/2 = 0$ s. Examples of two-time intensity-intensity correlation functions are shown in Fig. 3(a).

For a quantitative analysis, 'aged' one-time intensity-intensity correlation functions were used. These were obtained from $G$ as [74,76,77]:

$$g_2(Q, \Phi, t_{age}, \tau) = \langle \frac{\langle I(t_{age} - \frac{\tau}{2}) \cdot I(t_{age} + \frac{\tau}{2}) \rangle_{Q,\Phi}}{\langle I(t_{age} - \frac{\tau}{2}) \rangle_{Q,\Phi} \cdot \langle I(t_{age} + \frac{\tau}{2}) \rangle_{Q,\Phi}} \rangle_{t_{age}},  \quad (2)$$

with lag time $\tau = |t_2 - t_1|$, average 'age' $t_{age} = (t_1 + t_2)/2$ and where the average $\langle....\rangle_{t_{age}}$ is taken over a small time interval $t_{age} \pm \Delta t_{age}$ over which $G$ describes quasi-stationary (that is age-independent) dynamics.

This is effectively taking a "slice" of the two-time intensity correlation function, extending perpendicular from the $t_1 = t_2$ diagonal, with width $2\Delta t_{age}$. (see Fig. 3a)) As seen in previous work on colloidal systems [77], the one-time intensity correlation function is well-modelled by the Kohlrausch-Williams-Watts (KWW) form [74]:

$$g_2(Q, \Phi, t_{age}, \tau) = 1 + \beta e^{-2(\tau/\tau_0)^\gamma}, \qquad (3)$$

where $\beta$ is a contrast factor which depends on the experimental setup. It might be smaller than the contrast $\beta_0$ observed for a static reference sample, if the sample exhibits dynamic modes faster than the minimum lag time ($\tau$) accessible in the experimental setup ($\beta_0 \approx 0.17$–0.18 in this study, determined by a static porous glass sample, CoralPor®, SCHOTT), $\tau_0$ is the characteristic relaxation time and $\gamma$ is the stretching/compression exponent. Examples of aged one-time intensity-intensity correlation functions and their fits according to Eq. (3), are shown in Fig. 3(b).

The $\gamma$ exponent characterizes the overall dynamics, in that $\gamma = 1$ corresponds to Brownian diffusion while $\gamma < 1$ and $\gamma > 1$ describe sub-diffusive and hyper-diffusive dynamics respectively [78,79]. Right upon deposition of the filament, the nanoscale evolution is governed by sub-diffusive dynamics ($\gamma < 1$), that around $t_{age} \approx 5$ s (see Fig. 3(d)) transitions to become hyper-diffusive ($\gamma > 1$). After reaching peak values of $\gamma \approx 1.75$ around $t_{age} \approx 10$ s, $\gamma$ trends towards values around 1.5 for $t_{age} \geq 400$ s. The observed evolution of $\gamma$ as a function of $t_{age}$ was found to be largely independent of Q and filament height $h$ and only differs marginally between the deposition and extrusion direction. A Q-independent value of $\gamma = 1.5$ is consistent with the hypothesis that the structural dynamics at later ages ($t_{age} \geq 400$ s) stems from relaxation processes of internal stresses built up in the material and which can cause a complete decay of the dynamic structure factor even for a fully developed solid [47,80,81]. Such Hyper-diffuse dynamics, characterized by $\gamma > 1$ is a common feature in the aging regime of soft condensed matter systems [80–85]. Transitions from $\gamma < 1$ to $\gamma > 1$ on time scales in the range $t_{age} \approx 10$–100 s were observed in previous studies during the printing of colloidal gels [67,68,69,71] and interpreted as the recovery of the gel from the shear thinning experienced during extrusion and deposition.

From the contrast $\beta$, obtained by a fit of the correlation functions according to Eq. (3), the presence of initial fast dynamics on time scales shorter than those accessible in this experiment can be evidenced from $\beta < \beta_0$. Since the contrast obtained for the ink sample is smaller than $\beta_0$ for the static reference sample, some decorrelation must have occurred on timescales faster than the minimum lag-time of 1.34 ms covered by the data series.

It is well known [50,76,84,86–90] that in dense colloidal suspensions semi-localized fast particle motions, like the localized rattling of particles within a 'cage' formed by nearest neighbor particles, causes non-ergodic dynamics. The intermediate scattering function $F(Q, \tau) = \sqrt{(1 - g_2(Q, \tau)/\beta_0)}$ decays to an initial plateau value of $\sqrt{\beta/\beta_0}$, the so-called non-ergodicity factor, before other relaxation processes, such as structural relaxation of internal stresses at larger $\tau$ cause $g_2(Q, \tau) \to 1$. The ergodicity factor provides a measure of the degree of structural arrest on short timescales and takes the form of a Debye-Waller factor:

$$\beta/\beta_0 = f_0^2 \exp\left(-\frac{1}{3}Q^2 r_0^2\right), \qquad (4)$$

with the fraction $f_0$ of particles whose dynamics is localized in rapid motions restricted to the localization length $r_0$. By fitting this functional form, the localization length $r_0$ of the fluctuations and the localized particle fraction $f_0$ were determined for each height, direction and $t_{age} < 10$ s (at larger $t_{age}$ the deviation of $\beta$ from $\beta_0$ became negligible). Fig. 4 shows the evolution of $r_0$ and $f_0$ with av-

erage age at the location of the measurements within the filament, as well as representative data and fits to Eq. (4).

As a general trend, the localization length $r_0$ decreases with increasing $t_{age}$, which is indicative of the ink's storage modulus $G'$ increasing upon ink deposition [77,87,91]. Near the substrate ($h \approx 33$ μm), the localization length in the deposition direction is significantly smaller than in the rest of the filament. This observation implies that the ink-substrate interaction affects the nanoscale dynamics by suppressing the fast dynamic modes quicker than in the bulk of the filament, or in other words, $G'$ recovers faster or is less affected by the complex shear profile the ink experiences during extrusion and deposition. In the extrusion direction $\beta/\beta_0 \approx 1$, for $h \approx 33$ μm (near the substrate), thus no localization length could be determined, meaning that this mode of dynamic motion – localized rattling – is suppressed by the interaction with the substrate in the extrusion direction. Apart from the substrate, the center of the filament ($h \approx 270$ μm) is distinctly different in that $r_0$ remains $>200$ Å up to $t_{age} \approx 6$ s, for both directions. At this height, the X-ray beam is probing predominantly the bulk of the filament, which is least affected by substrate and free surface effects. Interestingly, this distinction between bulk and surface/interface of the filament is also observed in the fraction of localized particles $f_0$, which is between 0.8–1.0 in most parts of the filament over the range of ages covered by the data, whereas in the center of the filament $f_0$ is slightly lower at around 0.6–0.7.

For the studied ink, the measured dependence of the relaxation time $\tau_0$ on Q is $\tau_0 = (v_d \cdot Q)^{-1}$, where $v_d$ is the drift velocity characterizing the dynamics [81]. Such linear Q-dependence of the relaxation time, often in combination with hyper-diffusive ($\gamma > 1$) dynamics is commonly observed in jammed soft condensed matter systems, such as concentrated colloidal gels and emulsions [80,81,84].

The drift velocity was determined for both principle directions (extrusion vs. deposition), filament height ($h$) and average sample age after deposition ($t_{age}$). Maps of the drift velocity, bilinearly interpolated for the entire range of heights and ages are shown in Fig. 5(a-b). Note that the distribution displayed here in the drift velocity maps corresponds to the dynamics of the particles, and not to the amount of the particles. The maps for both directions show a near height independent drift velocity at early ages, with values decreasing faster at the filament-air ($h \approx 500$ μm) and filament-substrate ($h \approx 0$ μm) interfaces. For $t_{age} > 100$ s the profiles show higher values of $v_d$ around $h \approx 100$–200 μm, while in particular in the deposition direction significantly lower values are observed near the substrate ($h \approx 33$ μm), compared to any other height for 100 s $< t_{age} <$ 250 s. This trend is reversed at later ages, for which $v_d$ is larger near the substrate compared to the rest of the filament. A possible explanation for this time- and spatial evolution of $v_d$ is interaction between the ink and the substrate, which might initially speed up the recovery of the ink's gel structure upon deposition, whereas at later ages pinning between the ink and the substrate hinder the structural relaxation, whereas the other parts of the filament are more free to adapt for instance to the volume changes accompanying the solvent evaporation. Such substrate effects, which depend on the ink's surface tension and the substrate's surface energy and mechanical properties, were previously observed for colloidal inks [71]. Overall, at any given age and height, the values of $v_d$ are slightly larger in the deposition direction than in the extrusion direction, which might be indicative of some settling of the filament. Within the model of dipole stress relaxation, $v_d$ is proportional to the rate of change of the stress source strength and the number of active stress sources [80]. At the slow extrusion/deposition speed (0.5 mm s$^{-1}$) in this study, the stresses associated with filament settling appear thus to be dominant in the 'aging regime' ($t_{age} \geq 400$ s), compared to the stresses induced in the sample during extrusion and deposition. Note that
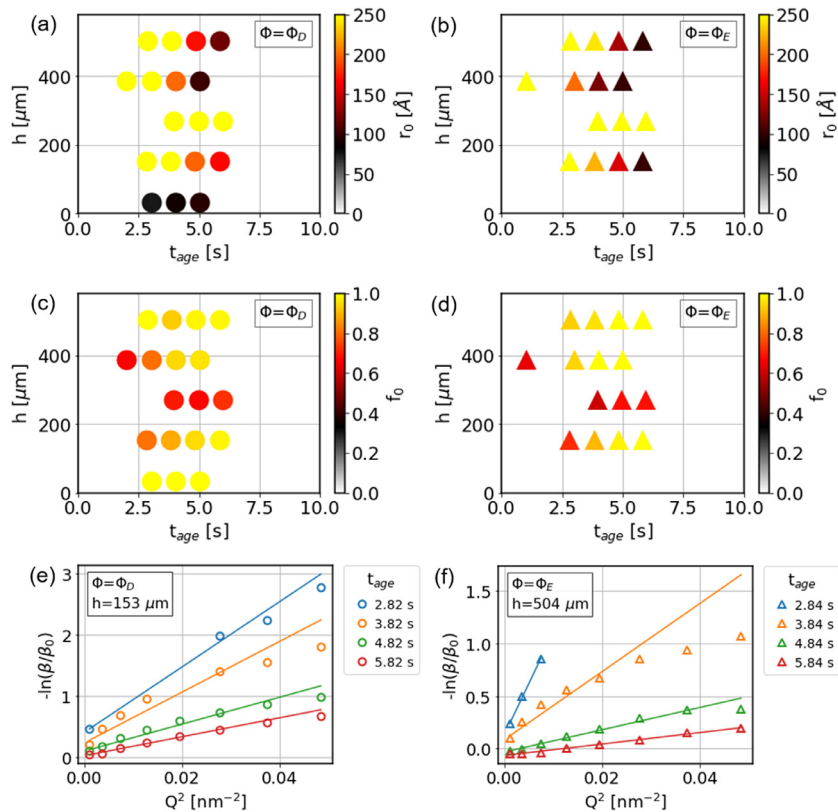
**Fig. 4.** (a), (b) Localization length $r_0$ of the early age fast dynamics for the deposition ($\Phi_D$) and extrusion ($\Phi_E$) directions as a function of age $t_{age}$ and filament height $h$. (c), (d) fraction $f_0$ of localized particles. Note that in the extrusion direction $\beta/\beta_0 \approx 1$, for $h \approx 33$ μm (right above the substrate), thus no localization length could be determined. (e), (f) examples of data and fits according to Eq. (4).
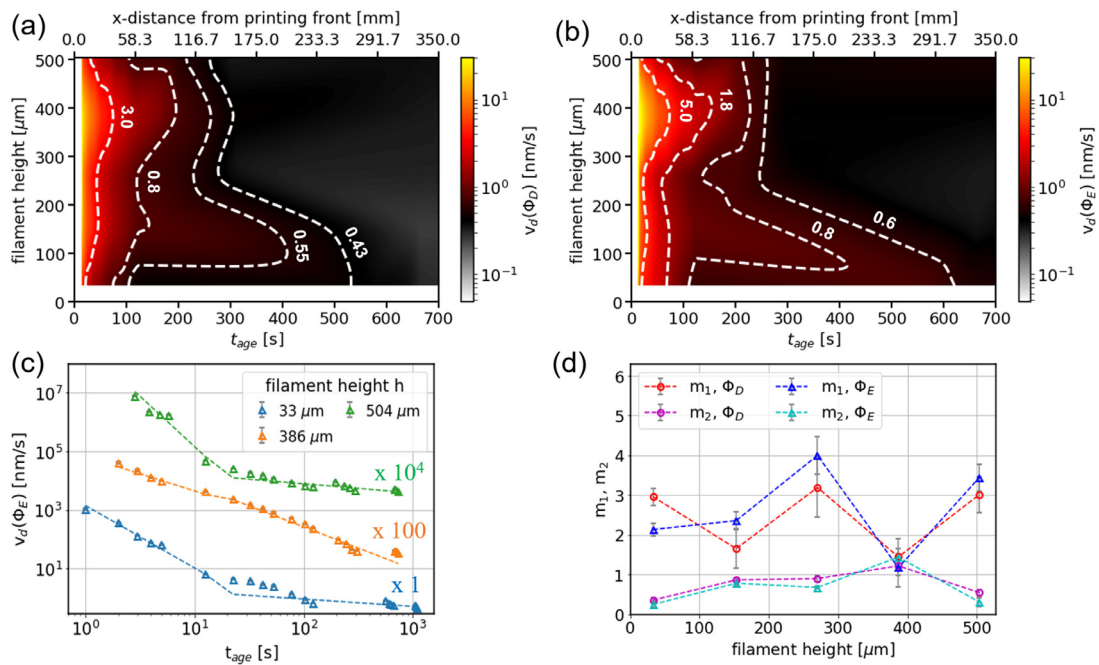


**Fig. 5.** Drift velocity interpolated for the entire range of filament heights and ages for (a) the deposition ($\Phi_D$) and (b) the extrusion ($\Phi_E$) directions, respectively. (c) Log-log plot of the time dependence of $v_d$ with the split power law fits for three selected filament heights in the extrusion ($\Phi_E$) direction. Data has been shifted along the y-axis by factors of 1 ($h = 33$ μm), 100 ($h = 386$ μm), and $10^4$ ($h = 504$ μm). (d) Power law exponents $m_1$ and $m_2$ for all heights and both directions.

the stresses associated with extrusion are originally along the extrusion direction; however, the filament undergoes a 90° turn during deposition, so these stresses should to a large degree end up in along the deposition direction as well, due to the interaction with the substrate and the viscosity of the ink. The observed spatiotemporally heterogeneous solidification profile showed a faster slowing-down rate in the dynamics at the surface of the printed filament as well as the interface between the printed filament and the substrate. Since the extrusion and deposition are both highly time-dependent processes, the time scale of the slowing-down dynamics shown in Fig. 5(a-b) is thus a critical consideration while printing larger multi-filament structures of the electrodes. Especially at the region of the filament-filament interface, mobile particles with high drift velocity are required to assist the interlayer diffusion to maintain the continuity of the structure [92]. This structural continuity is necessary to provide good electrical and ionic conductivities for a 3D-printed electrode to facilitate its electrochemical function.

The time dependence of the drift velocity for a particular height is well-described by a split power law with two different exponents for different time regimes, $m_1$ and $m_2$: $v_d \propto t_{age}^{-m_i}$ with $i = 1$ for $t_{age} < t_c$ and $i = 2$ for $t_{age} > t_c$, respectively. Remarkably, this model fits the data well with the same transition time $t_c \approx 13$ $s$ for each height, suggesting a transition between two mechanisms.

Generally, the initial decay of $v_d$ is faster than the subsequent decay ($m_1 > m_2$). The notable exception to this is that for the 2nd height measured from the top of the printed filament ($h = 386$ μm), the data is consistent with a single power law (the second exponent is within one standard deviation of the first exponent). These findings are shown in Fig. 5(c). The height dependence of the power-law exponents $m_1$ and $m_2$ are shown for both directions in Fig. 5(d). Except for the above-mentioned height of 386 μm, the power-law exponent $m_1$ of the initial decay is generally larger than that of the second decay ($m_2$), by up to a factor of 4. Notably, the transition time $t_c$ is quite similar to the timescales on which the compression exponent $\gamma$ reaches its maximum value and the localization length $r_0$ decreases to near zero. Overall, the data supports the existence of two distinct relaxation mechanisms dominating the dynamics at different ages. Such combination of a fast and slow relaxation mechanism has been reported for colloidal glasses and gels [81,83,85,93] as well as for a colloidal gel undergoing UV curing during in-situ 3D printing [67]. In these studies, the slower relaxation process for large $t_{age}$ followed a power-law dependence with exponents between about 0.4 and 1.5 originating from aging processes, involving slow, cooperative rearrangement events on the nanoscale. In this study, $m_2 \approx 1$ in the bulk of the filament, corresponding to a full-aging behavior [82]. Contrary, 0.24 $< m_2 < 0.58$ near the bottom and the top of the filament, thus the ink exhibits sub-aging near the interfaces.

In order to determine whether the fast relaxation mechanism is driven by solvent evaporation, we tracked the weight of a deposited filament by means of a semi-micro balance (Mettler Toledo AB135-S/FACT). The weight loss corresponds to the evaporation of water, as this is the only ink component with relevant vapor pressure at room temperature. Based on the known composition of the ink, the weight loss for waiting times ($t_w$) $\leq t_c$ is estimated to reduce the water content of the ink (around 33 wt.%) by <0.1 wt.% (see Fig. S 6). This small compositional change cannot be the main cause for the observed slowing of the dynamics by more than two orders of magnitude over the same time interval. We therefore attribute the first relaxation mechanism to the recovery of the structure from the shear force that the filament experienced during extrusion and deposition. Within the $t_w$ covered by the experiment, the water content of the ink reduces to about 29 wt.% due to evaporation and this change in composition likely contributed to the second, slower relaxation process.

The slowing of the dynamics for $t_{age} \geq 400$ s where $\tau_0 \propto Q^{-1}$ and $\gamma \approx 1.5$ can be interpreted as a decrease in the rate of change of the stress source strength, or by a change in the number of active stress sources [80]. With the relaxation of stresses in the material through local reorganizations, new stress sources might be created with a longer lifetime, thereby giving rise to longer relaxation times and smaller displacement velocities. In addition, the sample might still undergo some hardening at these ages due to ongoing evaporation of solvent (water).

The ink in this study is a colloidal system with high volume fraction of nanoparticles. For ages beyond the initial fast decrease in $v_d$ ($t_{age} \geq 10$ s) the ink dynamics has similar characteristics as the ones found for colloidal gels, namely slow relaxations via ballistic-like structural re-arrangements that obey a non-diffusive $\tau_0 \propto Q^{-1}$ relationship [80,90,94]. Solvent evaporation after the deposition might cause volumetric shrinkage, thus further increasing the particle volume fraction and driving the system towards a jammed state, where the dynamics is dominated by stress relaxation processes, that might lead to temporally heterogeneous dynamics [95]. Generally, dynamical heterogeneities are caused by random rearrangement events of subdomains of the sample, when the number of statistically independent objects becomes less than the number of particles, as discussed for instance for colloidal gels [77]. Such temporally heterogenous dynamics can be characterized by the normalized variance of the instantaneous degree of correlation [74]:

$$\chi(Q, \Phi, t_{age}, \tau) = \frac{\langle G^2(Q, \Phi, t_{age}, \tau) \rangle_{t_{age} \pm \Delta t_{age}} - \langle G(Q, \Phi, t_{age}, \tau) \rangle^2_{t_{age} \pm \Delta t_{age}}}{[g_2(Q, \Phi, t_{age}, \tau = 0) - 1]^2}, \quad (5)$$

$\chi$s are being calculated over a range of $t_{age} + \Delta t_{age}$ for which the dynamics is approximately stationary, that is $\tau_0 \approx const$. Fig. 6(a) shows an example of dynamical heterogeneities along the deposition direction for $Q = 0.00326$ $Å^{-1}$ (corresponding to a length scale of approximately 190 nm) at height $h = 33$ μm above the substrate.

Dynamical heterogeneities were identified by the presence of a peak in $\chi$ for ages in the time-window 200 $s < t_{age}$ 300 $s$, where the dynamics is stationary enough (see Fig. 6(b)) to rule out significant contributions to $\chi$ from evolving timescales of the dynamics. While at the bottom ($h = 33$ μm) and top ($h = 504$ μm) of the filament dynamic heterogeneities were also identified at ages $> 500$ s, they appear to the absent for intermediate heights. Due to the geometry of the scattering experiment, the scattering signal when probing the top or bottom of the filament predominantly stems from the outer layer of the filament, while the filament bulk dominates the signal when probing the heights in between (see Fig. 1 for the experimental setup). Thus, such finding could point towards the existence of an outer (skin-) layer and/or a substrate effect, where the filament exhibits different viscoelastic properties close to its outer perimeter compared to the bulk. However, it is noteworthy that each measurement at a different height requires the deposition of a new filament, thus it is in principle possible that the time window in which the dynamic heterogeneities occur shows some degree of variation from filament to filament. Nevertheless, the occurrence of dynamical heterogeneities is reproducible and thus can be considered to be an inherent part of the relaxation process during filament solidification.

For the identified dynamical heterogeneities, the position $\tau^*$ of the peak $\chi^*$, determined from a fit with an asymmetric pseudo-Voigt profile [96], is comparable with the relaxation time $\tau_0$ within about a factor three (Fig. 6(c)) and follows the same $Q^{-1}$ dependence. This supports the supposition that random rearrangements of larger sample subdomains, rather than rearrangements on the single particle level, take over as the dominant mode of structural decorrelations after a certain filament age. The onset of dynamic
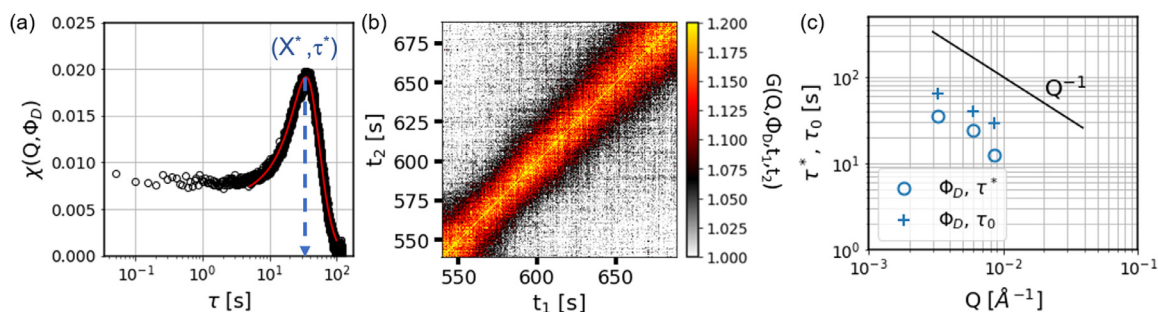
**Fig. 6.** (a) Normalized $\chi$ and $g_2$ as a function of lag time $\tau$ ($h = 33$ µm, $Q = 0.00326$ $Å^{-1}$, deposition direction). A clear peak is visible roughly around $\tau = 35$ s indicating the presence of dynamical heterogeneities. Red solid line is a fit to an asymmetric pseudo-Voigt profile, used to determine peak height $\chi^*$ and position $\tau^*$. (b) Corresponding two-time correlation-correlation function, showing quasi-stationary dynamics. (c) Comparison of the relaxation time $\tau_0$ and the position $\tau^*$ of the peak $\chi^*$ of the dynamical heterogeneity, both following the same $Q^{-1}$ dependence.
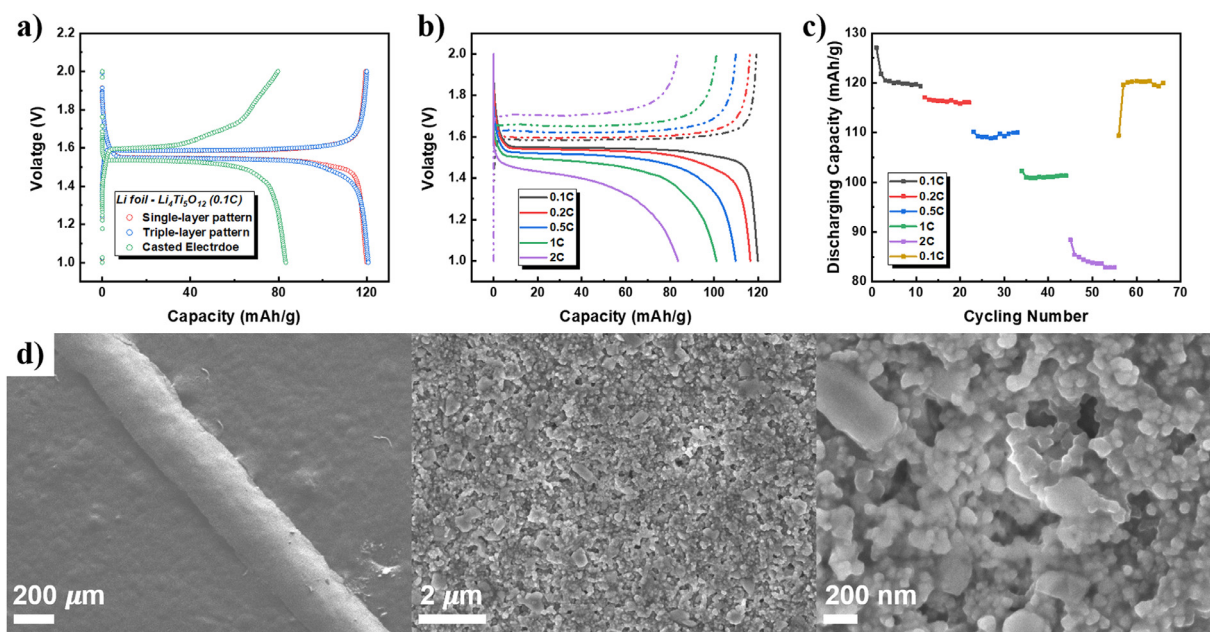


**Fig. 7.** (a) The representative discharge-charge curves of printed and casted electrodes with 0.1C cycling rate. (b) and (c) Rate-dependent cycling performance of printed single layer electrode from 0.1C, 0.2C, 0.5C, 1C, 2C and back to 0.1C. (d) The surface morphology of the printed electrodes shown by SEM images at different magnification.

heterogeneities can be possibly linked to the sample transitioning from a liquid-like state right upon deposition, to a more solid-like state that can accumulate microscopic stresses that eventually get released in abrupt mesoscopic rearrangement events. This phenomenon can lead to an inhomogeneous particle distribution and a locally uneven stress/strain distribution that cause the formation of defects such as voids and cracks in the printed structures [71]. Such cracks have been found to impact the performance of batteries in a complex way: it is possible that they contribute towards the degradation of the electrodes, leading to capacity fades, but they also could potentially facilitate the ionic diffusion within the electrodes, thereby enhancing the rate capability [97]. Moreover, the transition to these mesoscopic rearrangement events is driven by the rheological properties of the ink, recovering its gel structure after being shear-thinned during extrusion, and the evaporation of the high vapor pressure solvent (water) after filament deposition. As the solvent evaporates during the printing process, the materials are arrested in an intermediate state, which could lead to residual stresses. These residual stresses may cause crack formation later during the electrochemical cycling. The dynamical heterogeneity thus provides us insights to probe the onset of the potential defect formation during printing. While the observed dynamic heterogeneities are relatively small, they may be connected to larger meso– to macroscale rearrangement effects such as the

inhomogeneity of particle distribution and the residual stress, and might ultimately lead to the formation of structural defects in the printed filament [71].

## 3.3. Electrochemical performance testing

To demonstrate the electrochemical performance of the synthetic ink, LTO half cells were fabricated with two types of electrodes: 1) blade-casted ink on current collectors, for testing the baseline performance of the ink without printed pattern and 2) direct extrusion printing on lower coin cell casings with 1 and 3 layer structures. The cycling profiles and rate performance of the two types of electrodes were examined within the voltage window of 2.0–1.0 V and are shown in Fig. 7. Fig. 7(a) shows the discharge-charge curves of printed electrodes versus casted electrodes cycled at 0.1C. The printed single and triple layer electrodes delivered ~120 mAh g$^{-1}$ charging/discharging capacity and have a better agreement with the theoretical capacity of LTO, 175 mAh g$^{-1}$, than the casted ones, which delivered a slightly lower capacity of 83.2 mAh g$^{-1}$, under 0.1C rate. Fig. 7(b) and (c) presents the rate-dependent cycling performance of a single layer electrode with various C rates in the sequence: 0.1C, 0.2C, 0.5C, 1C, 2C and back to 0.1C. The 3D printed electrodes demonstrated a good electrochemical cycling performance at different rates where casted electrodes

cannot be fabricated with the same thickness as printed electrodes. The surface morphology of the printed electrodes was examined by SEM (Fig. 7(d)), which showed that they retained their structural integrity upon electrochemical cycling. The stable printing structure and good cycling performance show the improvement of electrochemical performance and enhance the potential of additive manufacturing in electrode synthesis. The better performance of the printed electrode is likely mainly due to the higher active material utilization. The casted ink is a uniform film casted by a blade gap of 200 μm, which is the same as the nozzle size but is relatively thick compared to conventional casted electrodes (tens of microns in thickness). Therefore, the amount of accessible active materials is believed to be lower in the casted electrode than in the printed structure. This is because the printed pattern provides better accessible ionic diffusion pathways. In conjunction with the different amount of material utilization, the dynamics of a thin film electrode during casting and curing, as well as the resulting structure could also differ from a printed structure, thereby further contributing to the varying electrochemical performance. Studying the dynamics of the casting process via XPCS can be a future research direction to further understand the origin of this processing-structure-property correlation. Overall, with further understanding of the dynamic structural evolution during printing, an optimal 3D-printed battery could be realized by designing the electrode materials, ink synthesis, and printing variables tailored for specific applications.

## 4. Conclusion

In this work a 3D printing ink with a viscosifier for the use in the printing of energy storage devices was prepared and investigated. Rheological testing confirmed the necessary shear-thinning property of the ink and ascertained that it recovers its gel structure after deposition. The cluster size distribution of the active functional component, LTO, was found to be uniform with some small aggregates.

Based on the behavior of the stretching exponent in the KWW form describing the one-time correlation function, the dynamics can be characterized as hyper-diffusive after the transition from sub-diffusive dynamics at sample age of around 5 s. The observed KWW fitting is consistent with the relaxation of internal stresses built up in the deposited material.

Evidence for initial fast dynamics on time scales shorter than those accessible in this experiment is found from the comparison of the reference contrast factor to the initial contrast factor in the KWW form fit to the one-time correlation function. This initial decorrelation, interpreted as semi-localized fast particle motions within a nearest neighbor particle "cage", was characterized by a spatiotemporally resolved localization length and a localized particle fraction. The results suggest a distinction between bulk and surface/interface of the filament – the rattling motion is suppressed near the substrate, likely due to substrate-ink interaction, while the localization length in the middle of the sample decreases slower than the general trend for all heights.

It was found that the wave vector is inversely proportional to the relaxation time, along with a stretching factor of around 1.5, which is a typical indicative of jammed soft condensed mater systems. The proportionality constant – the drift velocity – was calculated for all heights and sample ages and then interpolated to produce spatiotemporally resolved velocity dispersion maps for each direction. These maps show near height-independent velocity dispersion at early sample ages with higher velocity dispersion near the substrate at later sample ages, again suggesting the significance of the substrate-ink interaction.

The time dependence of the drift velocity was found to be well-described by a split power law with an initial decay generally

faster than the subsequent decay. Notably, the transition time between the two modes of velocity dispersion decay is the same for different heights and directions. This constitutes evidence for the existence of two distinct relaxation mechanisms.

By analyzing dynamic susceptibility – the normalized variance of the instantaneous degree of correlation – the presence of dynamic heterogeneities at specific times and heights was found. A peak in dynamic susceptibility not associated with changing time scales of the dynamics indicates a random rearrangement event of subdomains of the sample. Since the occurrence of these dynamic heterogeneities was found to be reproducible, they must be inherent to the relaxation process.

Electrodes fabricated with the investigated ink showed good performance in cycling at different rates. Characterization of the surface morphology of the electrodes through SEM indicated that the electrodes retained structural integrity even after electrochemical testing. A comparison between casted and printed electrodes demonstrated the potential for improving electrochemical performance through the deliberate design of the battery architecture by a specific printing pattern. The anisotropic dynamics, spatiotemporally heterogeneity, and rearrangement of subdomains revealed by XPCS showed the impact a highly anisotropic, far-from equilibrium processing method such as 3D printing can have on the nano- to meso–scale structure of the electrode. These events play important roles in the interaction among the active materials, conductive agents, and viscosifiers, and thus impact the defect formation, the mechanical stability, and the electrochemical functionality. Therefore, understanding the nano- to meso–scale dynamics of deposited structures during the printing process has the potential to enable rational designs of 3D printed energy storage devices with tailored internal structures. However, future work is needed to further connect the nano-/meso–scale dynamics with the electrochemical performances, such as by establishing fundamental physics models that could parametrize the complex engineering printing process, as well as by further characterizing the resulting structures of the printed electrodes. Notably, the dynamic properties can be highly composition-dependent and may vary in different battery materials. With the rising demands of next generation batteries, such as high mass-loading electrodes, fast charging-discharging capability, aqueous electrolytes for enhanced safety and solid-state batteries, various printing inks and more complex printing structures are required. Further work is also needed to make direct quantitative comparison of XPCS analysis results between different types of ink-deposition techniques. It might even be possible to obtain comparative results for blade-casted electrodes using a grazing scattering geometry. The understanding of how different battery fabrication methods manifest themselves in the characteristics of the dynamics that governs the mesoscale structure formation could further guide the design of batteries. Thus, we hope that this work is the beginning of fundamentally understanding the dynamic evolution of printing structures to enable the design of the ink and printable battery properties.

Overall, the far-from-equilibrium processes involved in 3D printing of energy storage devices were characterized in detail for a specific 3D printing ink used to fabricate working batteries. This characterization has implications for the informed fabrication of high-performance energy storage devices that are both direct – a) the spatiotemporally heterogenous solidification profile, as observed in the velocity dispersion maps, suggests that understanding filament-substrate and filament-filament interactions is crucial to fabricating complex multi-filament architectures and b) meso– to macroscale rearrangement events investigated through the analysis of dynamic susceptibility could be related to defect formation in the printed filament which is known to affect the electrochemical performance – and indirectly – the mesoscale structure and, by extension, the electrochemical performance of a 3D printed energy

storage device is at least in part determined by the first step in its fabrication, the printing process. The results of this study motivate further investigations of the dynamics of the 3D printing of energy storage devices to firstly, disentangle the observations that generally apply to similar soft matter systems and the observations that are particular to the used ink composition and manufacturing process and, secondly, to establish and further connections between the 3D printing dynamics and mesoscale structure formation (and ultimately, the electrochemical performance of the energy storage device).

## Declaration of Competing Interest

The authors declare that they have no known competing financial interests or personal relationships that could have appeared to influence the work reported in this paper.

## Acknowledgments

## Author Contributions

Y-cK Chen-Wiegart, L Wiegart, and C-H Lin developed the research concept with inputs from K Sun. C-H Lin, L Wiegart, and Y-cK Chen-Wiegart designed the synchrotron scattering experiment. C-H Lin and O Chen fabricated the 3D printing ink under the guidance of K Sun. C-H Lin and O Chen conducted the rheology measurements. B Zheng conducted the dynamic light scattering experiment under the supervision of S Bhatia. C-H Lin, D Yen, and Q Meng performed the SEM analysis. C-H Lin, O Chen, and Q Meng printed the electrodes for *ex situ* characterization. C-H Lin, K Sun, and Q Meng assembled the electrochemical cells and performed the cycling tests. L Wiegart developed the *in situ* printing setup at the CHX beamline, and set up the CHX beamline for the experiment. L Wiegart, C-H Lin, O Chen, K Sun, Q Meng, and Y-cK Chen-Wiegart conducted the *in situ* XPCS experiments with other CHX beamline staff members and Chen-Wiegart group members. K Dyro, C-H Lin, and O Chen performed the XPCS data analysis under the guidance of L Wiegart and Y-cK Chen-Wiegart; L Wiegart also performed further XPCS data analysis associated with the early age fast dynamics. C-H Lin, K Dyro, O Chen, and D Yen wrote the manuscript under the supervision of L Wiegart and Y-cK Chen-Wiegart, with the inputs from all co-authors.

## Data availability

The raw data required to reproduce these findings cannot be shared at this time as the data also forms part of an ongoing study. The processed data required to reproduce these findings cannot be shared at this time as the data also forms part of an ongoing study.

## Credit Author Statement

Cheng-Hung Lin: Conceptualization, Methodology, Software, Formal Analysis, Investigation, Writing – Original Draft, Visualization. Karol Dyro: Software, Formal analysis, Writing – Original Draft, Visualization. Olivia Chen: Software, Investigation, Formal analysis, Writing – Original Draft, Visualization. Dean Yen: Investigation, Formal analysis, Writing – Original Draft, Visualization. Bingqian Zheng: Investigation. Maria Torres Arango: Investigation. Surita Bhatia: Supervision. Ke Sun: Conceptualization, Investigation, Supervision. Qingkun Meng: Investigation. Lutz Wiegart: Conceptualization, Methodology, Software, Validation, Formal analysis, Investigation, Resources, Data Curation, Writing – Reviewing & Editing, Visualization, Supervision. Yu-chen Karen Chen-Wiegart: Conceptualization, Methodology, Formal analysis, Investigation, Resources, Writing – Reviewing & Editing, Supervision, Project administration, Funding acquisition

## Supplementary materials

Supplementary material associated with this article can be found, in the online version, at doi:10.1016/j.apmt.2021.101075.

## References

[1] M.L. Seol, R. Ivaskeviciute, M.A. Ciappesoni, F.V. Thompson, D.I. Moon, S.J. Kim, J.W. Han, M. Meyyappan, Nano Energy 52 (2018) 271–278, doi:10.1016/j.nanoen.2018.07.061.

[2] D.K. Patel, C. Bat-El, L. Etgar, S. Magdassi, Mater. Horiz. 5 (4) (2018) 708–714, doi:10.1039/c8mh00296g.

[3] T.S. Wei, B.Y. Ahn, J. Grotto, J.A. Lewis, Adv. Mater. 30 (16) (2018), doi:10.1002/adma.201703027.

[4] K. Sun, T.S. Wei, B.Y. Ahn, J.Y. Seo, S.J. Dillon, J.A. Lewis, Adv. Mater. 25 (33) (2013) 4539–4543, doi:10.1002/adma.201301036.

[5] F. Zhang, M. Wei, V.V. Viswanathan, B. Swart, Y.Y. Shao, G. Wu, C. Zhou, Nano Energy 40 (2017) 418–431, doi:10.1016/j.nanoen.2017.08.037.

[6] M.S. Saleh, J. Li, J. Park, R. Panat, Additive Manuf. 23 (2018) 70–78, doi:10.1016/j.addma.2018.07.006.

[7] A. Zhakeyev, P.F. Wang, L. Zhang, W.M. Shu, H.Z. Wang, J. Xuan, Adv. Sci. 4 (10) (2017), doi:10.1002/advs.201700187.

[8] X.C. Tian, J. Jin, S.Q. Yuan, C.K. Chua, S.B. Tor, K. Zhou, Adv. Energy Mater. 7 (17) (2017), doi:10.1002/aenm.201700127.

[9] P. Chang, H. Mei, S.X. Zhou, K.G. Dassios, L.F. Cheng, J. Mater. Chem. A 7 (9) (2019) 4230–4258, doi:10.1039/c8ta11860d.

[10] A. Izumi, M. Sanada, K. Furuichi, K. Teraki, T. Matsuda, K. Hiramatsu, H. Munakata, K. Kanamura, J. Power Sources 256 (2014) 244–249, doi:10.1016/j.jpowsour.2014.01.067.

[11] A. Izumi, M. Sanada, K. Furuichi, K. Teraki, T. Matsuda, K. Hiramatsu, H. Munakata, K. Kanamura, Electrochim. Acta 79 (2012) 218–222, doi:10.1016/j.electacta.2012.07.001.

[12] Y.K. Pang, Y.T. Cao, Y.H. Chu, M.H. Liu, K. Snyder, D. MacKenzie, C.Y. Cao, Adv. Funct. Mater. 30 (1) (2020) 22, doi:10.1002/adfm.201906244.

[13] K. Fu, Y.B. Wang, C.Y. Yan, Y.G. Yao, Y.A. Chen, J.Q. Dai, S. Lacey, J.Y. Wan, T. Li, Z.Y. Wang, Y. Xu, L.B. Hu, Adv. Mater. 28 (13) (2016) 2587 –+, doi:10.1002/adma.201505391.

[14] J.A. Lewis, Adv. Funct. Mater. 16 (17) (2006) 2193–2204, doi:10.1002/adfm.200600434.

[15] A.E. Jakus, S.L. Taylor, N.R. Geisendorfer, D.C. Dunand, R.N. Shah, Adv. Funct. Mater. 25 (45) (2015) 6985–6995, doi:10.1002/adfm.201503921.

[16] J.S. Park, T. Kim, W.S. Kim, Sci. Rep. 7 (2017) 10, doi:10.1038/s41598-017-03365-w.

[17] M.A. Skylar-Scott, J. Mueller, C.W. Visser, J.A. Lewis, Nature 575 (7782) (2019) 330 –+, doi:10.1038/s41586-019-1736-8.

[18] J.T. Muth, D.M. Vogt, R.L. Truby, Y. Menguc, D.B. Kolesky, R.J. Wood, J.A. Lewis, Adv. Mater. 26 (36) (2014) 6307–6312, doi:10.1002/adma.201400334.

[19] U. Kalsoom, P.N. Nesterenko, B. Paull, RSC Adv. 6 (65) (2016) 60355–60371, doi:10.1039/c6ra11334f.

[20] J.W. Sha, Y.L. Li, R.V. Salvatierra, T. Wang, P. Dong, Y.S. Ji, S.K. Lee, C.H. Zhang, J.B. Zhang, R.H. Smith, P.M. Ajayan, J. Lou, N.Q. Zhao, J.M. Tour, ACS Nano 11 (7) (2017) 6860–6867, doi:10.1021/acsnano.7b01987.

[21] C.W. Foster, M.P. Down, Y. Zhang, X.B. Ji, S.J. Rowley-Neale, G.C. Smith, P.J. Kelly, C.E. Banks, Sci. Rep. 7 (2017) 11, doi:10.1038/srep42233.

[22] G. Longoni, Chimica Oggi-Chem. Today 35 (2) (2017) 40–43.

[23] A.E. Jakus, E.B. Secor, A.L. Rutz, S.W. Jordan, M.C. Hersam, R.N. Shah, ACS Nano 9 (4) (2015) 4636–4648, doi:10.1021/acsnano.5b01179.

[24] Z.S. Wang, Q.E. Zhang, S.C. Long, Y.X. Luo, P.K. Yu, Z.B. Tan, J. Bai, B.H. Qu, Y. Yang, J. Shi, H. Zhou, Z.Y. Xiao, W.J. Hong, H. Bai, ACS Appl. Mater. Interfaces 10 (12) (2018) 10437–10444, doi:10.1021/acsami.7b19635.

[25] W. Yu, H. Zhou, B.Q. Li, S.J. Ding, ACS Appl. Mater. Interfaces 9 (5) (2017) 4597–4604, doi:10.1021/acsami.6b13904.

[26] J. Snyder, T. Fujita, M.W. Chen, J. Erlebacher, Nat. Mater. 9 (11) (2010) 904–907, doi:10.1038/nmat2878.

[27] J. Li, M.C. Leu, R. Panat, J. Park, Mater. Des. 119 (2017) 417–424, doi:10.1016/j.matdes.2017.01.088.

[28] Y.B. Wang, C.J. Chen, H. Xie, T.T. Gao, Y.G. Yao, G. Pastel, X.G. Han, Y.J. Li, J.P. Zhao, K. Fu, L.B. Hu, Adv. Funct. Mater. 27 (43) (2017), doi:10.1002/adfm.201703140.

[29] J.T. Hu, Y. Jiang, S.H. Cui, Y.D. Duan, T.C. Liu, H. Guo, L.P. Lin, Y. Lin, J.X. Zheng, K. Amine, F. Pan, Adv. Energy Mater. 6 (18) (2016) 8, doi:10.1002/aenm.201600856.

[30] A.J. Blake, R.R. Kohlmeyer, J.O. Hardin, E.A. Carmona, B. Maruyama, J.D. Berrigan, H. Huang, M.F. Durstock, Adv. Energy Mater. 7 (14) (2017) 10, doi:10.1002/aenm.201602920.

[31] J.W. Ding, K. Shen, Z.G. Du, B. Li, S.B. Yang, ACS Appl. Mater. Interfaces 9 (48) (2017) 41871–41877, doi:10.1021/acsami.7b12892.

[32] S.D. Lacey, D.J. Kirsch, Y.J. Li, J.T. Morgenstern, B.C. Zarket, Y.G. Yao, J.Q. Dai, L.Q. Garcia, B.Y. Liu, T.T. Gao, S.M. Xu, S.R. Raghavan, J.W. Connell, Y. Lin, L.B. Hu, Adv. Mater. 30 (12) (2018), doi:10.1002/adma.201705651.

[33] K. Shen, H.L. Mei, B. Li, J.W. Ding, S.B. Yang, Adv. Energy Mater. 8 (4) (2018), doi:10.1002/aenm.201701527.

[34] K. Fu, Y. Wang, C. Yan, Y. Yao, Y. Chen, J. Dai, S. Lacey, Y. Wang, J. Wan, T. Li, Adv. Mater. 28 (13) (2016) 2587–2594.

[35] J. Hu, Y. Jiang, S. Cui, Y. Duan, T. Liu, H. Guo, L. Lin, Y. Lin, J. Zheng, K. Amine, F. Pan, Adv. Energy Mater. 6 (18) (2016) 1600856, doi:10.1002/aenm.201600856.

[36] T.S. Wei, B.Y. Ahn, J. Grotto, J.A. Lewis, Adv. Mater. 30 (16) (2018) 1703027.

[37] J. Wang, Q. Sun, X. Gao, C. Wang, W. Li, F.B. Holness, M. Zheng, R. Li, A.D. Price, X. Sun, ACS Appl. Mater. Interfaces 10 (46) (2018) 39794–39801.

[38] G. Crabtree, G. Rublof, E. Takeuchi, Basic Research Needs For Next Generation Electrical Energy Storage, 2017.

[39] K. Fu, Y.G. Yao, J.Q. Dai, L.B. Hu, Adv. Mater. 29 (9) (2017) 20, doi:10.1002/adma.201603486.

[40] R.R. Kohlmeyer, A.J. Blake, J.O. Hardin, E.A. Carmona, J. Carpena-Nunez, B. Maruyama, J.D. Berrigan, H. Huang, M.F. Durstock, J. Mater. Chem. A 4 (43) (2016) 16856–16864, doi:10.1039/c6ta07610f.

[41] Y. Shmueli, Y.C. Lin, S. Lee, M. Zhernenkov, R. Tannenbaum, G. Marom, M.H. Rafailovich, ACS Appl. Mater. Interfaces 11 (40) (2019) 37112–37120, doi:10.1021/acsami.9b12908.

[42] A. Nogales, E. Gutiérrez-Fernández, M.C. García-Gutiérrez, T.A. Ezquerra, E. Rebollar, I. Šics, M. Malfois, S. Gaidukovs, E. Gēcis, K. Celms, G. Bakradze, Macromolecules 52 (24) (2019) 9715–9723, doi:10.1021/acs.macromol.9b01620.

[43] E.B. Trigg, N.S. Hmeidat, L.M. Smieska, A.R. Woll, B.G. Compton, H. Koerner, Additive Manuf. 37 (2021) 101729, doi:10.1016/j.addma.2020.101729.

[44] G. Brown, P.A. Rikvold, M. Sutton, M. Grant, Phys. Rev. E 56 (6) (1997) 6601–6612, doi:10.1103/PhysRevE.56.6601.

[45] A. Robert, J Appl Crystallogr 40 (2007) S34–S37, doi:10.1107/s0021889807009168.

[46] J. Lal, D. Abernathy, L. Auvray, O. Diat, G. Grubel, Eur. Phys. J. E 4 (3) (2001) 263–271, doi:10.1007/s101890170108.

[47] P. Kwasniewski, A. Fluerasu, A. Madsen, Soft Matter 10 (43) (2014) 8698–8704, doi:10.1039/c4sm01671h.

[48] C. Caronna, Y. Chushkin, A. Madsen, A. Cupane, Phys. Rev. Lett. 100 (5) (2008), doi:10.1103/PhysRevLett.100.055702.

[49] S.B. Dierker, R. Pindak, R.M. Fleming, I.K. Robinson, L. Berman, Phys. Rev. Lett. 75 (3) (1995) 449–452, doi:10.1103/PhysRevLett.75.449.

[50] H. Guo, J.N. Wilking, D. Liang, T.G. Mason, J.L. Harden, R.L. Leheny, Phys. Rev. E 75 (4) (2007), doi:10.1103/PhysRevE.75.041401.

[51] E.M. Herzig, A. Robert, D.D. van't Zand, L. Cipelletti, P.N. Pusey, P.S. Clegg, Phys. Rev. E 79 (1) (2009), doi:10.1103/PhysRevE.79.011405.

[52] Y. Shinohara, H. Kishimoto, N. Yagi, Y. Amemiya, Macromolecules 43 (22) (2010) 9480–9487, doi:10.1021/ma102095b.

[53] H.Y. Guo, S. Ramakrishnan, J.L. Harden, R.L. Leheny, Phys. Rev. E 81 (5) (2010), doi:10.1103/PhysRevE.81.050401.

[54] R.L. Leheny, Curr Opin Colloid Interface Sci 17 (1) (2012) 3–12, doi:10.1016/j.cocis.2011.11.002.

[55] R.L. Leheny, M.C. Rogers, K. Chen, S. Narayanan, J.L. Harden, Curr. Opin. Colloid Interface Sci. 20 (4) (2015) 261–271, doi:10.1016/j.cocis.2015.10.001.

[56] T. Hoshino, Y. Tanaka, H. Jinnai, A. Takahara, J. Phys. Soc. Japan 82 (2) (2013), doi:10.7566/jpsj.82.021014.

[57] R. Hernández, A. Nogales, M. Sprung, C. Mijangos, T.A. Ezquerra, J. Chem. Phys. 140 (2) (2014) 024909, doi:10.1063/1.4861043.

[58] A.C. Genix, J. Oberdisse, Curr. Opin. Colloid Interface Sci. 20 (4) (2015) 293–303, doi:10.1016/j.cocis.2015.10.002.

[59] R.A. Narayanan, P. Thiyagarajan, S. Lewis, A. Bansal, L.S. Schadler, L.B. Lurio, Phys. Rev. Lett. 97 (7) (2006) 075505, doi:10.1103/PhysRevLett.97.075505.

[60] S. Srivastava, A.K. Kandar, J.K. Basu, M.K. Mukhopadhyay, L.B. Lurio, S. Narayanan, S.K. Sinha, Phys. Rev. E 79 (2) (2009) 021408, doi:10.1103/PhysRevE.79.021408.

[61] E. Senses, S. Narayanan, A. Faraone, ACS Macro Lett. 8 (5) (2019) 558–562, doi:10.1021/acsmacrolett.9b00176.

[62] P. Akcora, S.K. Kumar, J. Moll, S. Lewis, L.S. Schadler, Y. Li, B.C. Benicewicz, A. Sandy, S. Narayanan, J. Ilavsky, P. Thiyagarajan, R.H. Colby, J.F. Douglas, Macromolecules 43 (2) (2010) 1003–1010, doi:10.1021/ma902072d.

[63] Y. Shinohara, H. Kishimoto, N. Yagi, Y. Amemiya, Macromolecules 43 (22) (2010) 9480–9487, doi:10.1021/ma102095b.

[64] F. Ehrburger-Dolle, I. Morfin, F. Bley, F. Livet, G. Heinrich, S. Richter, L. Piché, M. Sutton, Macromolecules 45 (21) (2012) 8691–8701, doi:10.1021/ma3013674.

[65] O. Bikondoa, D. Carbone, V. Chamard, T.H. Metzger, Sci. Rep. 3 (2013) 6, doi:10.1038/srep01850.

[66] L. Wiegart, G.S. Doerk, M. Fukuto, S. Lee, R. Li, G. Marom, M.M. Noack, C.O. Osuji, M.H. Rafailovich, J.A. Sethian, Y. Shmueli, M. Torres Arango, K. Toth, K.G. Yager, R. Pindak, Synchrotron Radiat. News 32 (2) (2019) 20–27, doi:10.1080/08940886.2019.1582285.

[67] B.M. Yavitt, L. Wiegart, D. Salatto, Z. Huang, M.K. Endoh, S. Poeller, S. Petrash, T. Koga, ACS Appl. Polym. Mater. 2 (9) (2020) 4096–4108, doi:10.1021/acsapm.0c00716.

[68] K.J. Johnson, L. Wiegart, A.C. Abbott, E.B. Johnson, J.W. Baur, H. Koerner, Langmuir 35 (26) (2019) 8758–8768, doi:10.1021/acs.langmuir.9b00766.

[69] M.A. Torres Arango, Y. Zhang, R. Li, G. Doerk, A. Fluerasu, L. Wiegart, ACS Appl. Mater. Interfaces 12 (45) (2020) 51044–51056, doi:10.1021/acsami.0c14743.

[70] K. Sun, T.S. Wei, B.Y. Ahn, J.Y. Seo, S.J. Dillon, J.A. Lewis, Adv. Mater. 25 (33) (2013) 4539–4543, doi:10.1002/adma.201301036.

[71] M. Torres Arango, Y. Zhang, C. Zhao, R. Li, G. Doerk, D. Nykypanchuk, Y.c.K. Chen-Wiegart, A. Fluerasu, L. Wiegart, Mater. Today Phys. 14 (2020) 100220, doi:10.1016/j.mtphys.2020.100220.

[72] S.K. Abeykoon, Y.G. Zhang, E.D. Dill, T.A. Caswell, D.B. Allan, A. Akilic, L. Wiegart, S. Wilkins, A. Heroux, K.K. van Dam, M. Sutton, A. Fluerasu, Ieee, 2016 New York Scientific Data Summit (Nysds) (2016) 10.

[73] M. Sutton, K. Laaziri, F. Livet, F. Bley, Opt. Express 11 (19) (2003) 2268–2277, doi:10.1364/oe.11.002268.

[74] A. Madsen, R.L. Leheny, H.Y. Guo, M. Sprung, O. Czakkel, New J. Phys. 12 (2010) 16, doi:10.1088/1367-2630/12/5/055001.

[75] A. Fluerasu, A. Moussaid, A. Madsen, A. Schofield, Phys. Rev. E 76 (1) (2007) 4, doi:10.1103/PhysRevE.76.010401.

[76] A. Duri, L. Cipelletti, Europhys. Lett. 76 (5) (2006) 972–978, doi:10.1209/epl/i2006-10357-4.

[77] V. Trappe, E. Pitard, L. Ramos, A. Robert, H. Bissig, L. Cipelletti, Phys. Rev. E 76 (5) (2007) 7, doi:10.1103/PhysRevE.76.051404.

[78] W.S. Jang, P. Koo, K. Bryson, S. Narayanan, A. Sandy, T.P. Russell, S.G. Mochrie, Macromolecules 47 (18) (2014) 6483–6490, doi:10.1021/ma500956b.

[79] H.Y. Guo, G. Bourret, M.K. Corbierre, S. Rucareanu, R.B. Lennox, K. Laaziri, L. Piche, M. Sutton, J.L. Harden, R.L. Leheny, Phys. Rev. Lett. 102 (7) (2009) 4, doi:10.1103/PhysRevLett.102.075702.

[80] L. Cipelletti, L. Ramos, S. Manley, E. Pitard, D.A. Weitz, E.E. Pashkovski, M. Johansson, Faraday Discuss. 123 (2003) 237–251, doi:10.1039/b204495a.

[81] L. Cipelletti, S. Manley, R.C. Ball, D.A. Weitz, Phys. Rev. Lett. 84 (10) (2000) 2275–2278, doi:10.1103/PhysRevLett.84.2275.

[82] M. Bellour, A. Knaebel, J.L. Harden, F. Lequeux, J.P. Munch, Phys. Rev. E 67 (3) (2003) 8, doi:10.1103/PhysRevE.67.031405.

[83] S. Kaloun, R. Skouri, M. Skouri, J.P. Munch, F. Schosseler, Phys. Rev. E 72 (1) (2005) 5, doi:10.1103/PhysRevE.72.011403.

[84] R. Bandyopadhyay, D. Liang, H. Yardimci, D.A. Sessoms, M.A. Borthwick, S.G.J. Mochrie, J.L. Harden, R.L. Leheny, Phys. Rev. Lett. 93 (22) (2004) 4, doi:10.1103/PhysRevLett.93.228302.

[85] A. Robert, E. Wandersman, E. Dubois, V. Dupuis, R. Perzynski, Europhys. Lett. 75 (5) (2006) 764–770, doi:10.1209/epl/i2006-10179-4.

[86] W. Vanmegen, S.M. Underwood, P.N. Pusey, Phys. Rev. Lett. 67 (12) (1991) 1586–1589, doi:10.1103/PhysRevLett.67.1586.

[87] A.H. Krall, D.A. Weitz, Phys. Rev. Lett. 80 (4) (1998) 778–781, doi:10.1103/PhysRevLett.80.778.

[88] O. Czakkel, A. Madsen, Epl 95 (2) (2011) 6, doi:10.1209/0295-5075/95/28001.

[89] R. Angelini, A. Madsen, A. Fluerasu, G. Ruocco, B. Ruzicka, Colloid Surf. A-Physicochem. Eng. Asp. 460 (2014) 118–122, doi:10.1016/j.colsurfa.2014.03.087.

[90] A. Jain, F. Schulz, I. Lokteva, L. Frenzel, G. Grubel, F. Lehmkuhler, Soft Matter 16 (11) (2020) 2864–2872, doi:10.1039/c9sm02230a.

[91] K.S. Schweizer, G. Yatsenko, J. Chem. Phys. 127 (16) (2007) 9, doi:10.1063/1.2780861.

[92] Y. Shmueli, Y.C. Lin, X. Zuo, Y. Guo, S. Lee, G. Freychet, M. Zherenkov, T. Kim, R. Tannenbaum, Gad. Marom, D. Gersappe, M.H. Rafailovich, Compos. Sci. Technol. 196 (2020) 108227, doi:10.1016/j.compscitech.2020.108227.

[93] R. Angelini, L. Zulian, A. Fluerasu, A. Madsen, G. Ruocco, B. Ruzicka, Soft Matter 9 (46) (2013) 10955–10959, doi:10.1039/c3sm52173g.

[94] L. Ramos, L. Cipelletti, Phys. Rev. Lett. 87 (24) (2001) 4, doi:10.1103/PhysRevLett.87.245503.

[95] L. Cipelletti, H. Bissig, V. Trappe, P. Ballesta, S. Mazoyer, J. Phys.-Condes. Matter 15 (1) (2003) S257–S262, doi:10.1088/0953-8984/15/1/334.

[96] A.L. Stancik, E.B. Brauns, Vib. Spectrosc. 47 (1) (2008) 66–69, doi:10.1016/j.vibspec.2008.02.009.

[97] Y.C.K. Chen-Wiegart, Z. Liu, K.T. Faber, S.A. Barnett, J. Wang, Electrochem Commun 28 (2013) 127–130, doi:10.1016/j.elecom.2012.12.021.